RSC Advances

PAPER

View Article Online
View Journal | View Issue

Cite this: *RSC Adv.*, 2023, **13**, 20816

Solvothermal synthesis of organoclay/Cu-MOF composite and its application in film modified GCE for simultaneous electrochemical detection of deoxyepinephrine, acetaminophen and tyrosine†

Edwige Mouafo-Tchinda,[ab] Justin Claude Kemmegne-Mbouguen, *[a] Charles Peguy Nanseu-Njiki,[b] Henrietta W. Langmi,[c] Chrispin Kowenje,[d] Nicholas M. Musyoka[e] and Robert Mokaya *[f]

An organoclay/copper-based metal–organic framework (MOF) composite was synthesized using a solvothermal method by growing a Cu-BTC (copper(II) benzene-1,3,5-tricarboxylate) MOF from a mixture of the MOF precursor solution in which various amounts of organoclay had been dispersed. The organoclay was obtained by intercalating a cationic dye, namely thionin, into a natural Cameroonian clay sampled in Sagba deposit (North West of Cameroon). The organoclay and the as-synthesized composites were characterized by X-ray diffraction (XRD), Fourier-transform infrared spectroscopy (FT-IR), scanning electron microscopy (SEM) and Brunauer, Emmett and Teller (BET) techniques. From Scherrer's equation, the crystallite size of the composite was found to be between 55 and 58 nm, twice as large as the pristine MOF's crystallite size. The organoclay/Cu-MOF composite (Sa-TN_{50}/$Cu_3(BTC)_2$) exhibiting a BET surface area of 192 m^2 g^{-1}, about twice that of pristine clay and about one seventh that of pristine MOF, was then utilized to form a stable thin film onto glassy carbon electrodes (GCE) by drop coating (Sa-TN_{50}/$Cu_3(BTC)_2$/GCE). These electrodes demonstrated electrocatalytic behavior toward deoxyepinephrine (DXEP) and thus enabled selective and simultaneous sensitive detection of three analytes: DXEP, acetaminophen (AC) and tyrosine (TYR) compared with bare GCE and clay modified electrode. Under optimum conditions, Sa-TN_{50}/$Cu_3(BTC)_2$/GCE exhibited good performance including large calibration curves ranging from 5.0 μM to 138.0 μM for DXEP, 4.0 μM to 153.0 μM for AC and 1.0 μM to 29.4 μM for TYR. The detection limits were found to be, 0.4 μM, 0.7 μM and 0.2 μM for DXEP, AC and TYR, respectively. The developed sensors have been applied successfully in the quantification of AC in a commercial tablet of AC, and DXEP, AC and TYR in tap water.

Received 9th June 2023
Accepted 5th July 2023

DOI: 10.1039/d3ra03850e

rsc.li/rsc-advances

1. Introduction

Clay minerals are natural layered aluminosilicates consisting of a tetrahedral and an octahedral sheet in either 1 : 1 or 2 : 1 configuration. Clays may be used in a variety of applications ranging from agriculture to surface coating and environmental use[1] because of their interesting features including, large specific area, good catalytic support properties, thermal stability and mechanical stability as well as low cost. Among clay materials, the smectite group which is a 2 : 1 phyllosilicate, has attracted considerable attention owing to its particle size, high surface area, ion exchange capacity, swelling property, chemical stability and thermal stability.[2] Smectites have been efficiently used for the removal from the environment of heavy metals[3] and dyes,[4,5] both of which are longstanding environmental pollutants.

Thanks to the attractive properties of smectites, they have also attracted much attention in the field of electrochemistry since the pioneering work of Gosh and Bard in 1983.[6] In order to improve selectivity and sensitivity as electrode modifiers, organic–inorganic hybrids namely organoclays, may be prepared *via* either grafting of specific organic moieties onto the clay surface or by intercalating organic species in the interlayer

[a]*Laboratory of Porous Materials for Sensors and Energy, Faculty of Science, University of Yaounde 1, P. O. Box 812, Yaoundé, Cameroon. E-mail: jkemmeg@yahoo.fr*
[b]*Laboratoire d'Electrochimie et de Génie des Materiaux, Faculté des Science, B. P 812, Yaoundé, Cameroon*
[c]*Department of Chemistry, University of Pretoria, Private Bag, X20 Hatfield, 0028, South Africa*
[d]*Department of Chemistry, Maseno University, P. O. Box, 333-40105, Maseno, Kenya*
[e]*Nanotechnology Research and Application Center (SUNUM), Sabanci University, Istanbul, 34956, Turkey*
[f]*School of Chemistry, University of Nottingham, University Park, Nottingham, NG7 2RD, UK. E-mail: r.mokaya@nottingham.ac.uk*

† Electronic supplementary information (ESI) available. See DOI: https://doi.org/10.1039/d3ra03850e

region of the clay. In such scenarios, the organic species also convert the interlayer space of smectites from hydrophilic to hydrophobic.[7,8] Organoclay and clay modified electrodes have been explored successfully as immunosensors, biosensors[9,10] and sensors[11,12] despite their insulating character which can be overcome by using redox mediators. The redox mediators are used for electroanalytical applications to either increase the electrochemical response or to decrease the overpotential, or both. The mediators, which can be organic or inorganic molecules, may be located within the clay[13] or in the interlayer region of the clay.[14]

Recently, other organic–inorganic porous materials, namely metal–organic frameworks (MOFs), have emerged as possible electrode modifiers in voltammetry determination of inorganic or organic species[11,15] although research in this area is still in the early stages.[16] Several routes for MOF synthesis have been reported including electrochemical synthesis, microwave assisted synthesis, sonochemical synthesis, mechanochemical synthesis, evaporation synthesis, microfluidic synthesis, and solvothermal synthesis. Among these MOFs preparation techniques, solvothermal synthesis appears to be the most preferable method, owing to the fast reaction kinetics, and production of uniform products with high phase purity and crystallinity.[17,18] MOFs display interesting physicochemical properties including high surface area, tunable pore size and good chemical reactivity.[16] By combining highly porous structures with a specific functional group, MOF modified electrodes can offer rapid diffusion of the analyte into their pores and thus improve framework–analyte interactions, which would enhance analyte detection. In addition to these interesting properties, MOFs exhibit good redox conductivity, which is enabled by their large porosity,[19] thus making them suitable for electrocatalytic reactions.[19,20] More recently, research is growing in the area of the synthesis of MOF composites with synergetic and new interesting properties such as exceptional electrochemical activity, conductivity and stability, thus overcoming low conductivity and lack of chemical stability encountered for pristine MOFs.[21] To date, MOF-based composites for electrochemical sensing have focused on MOF/carbon composites,[22–24] MOF/metal nanoparticle composites,[22] MOF/metal oxide composites,[22,25] MOF/polymer composites,[22] MOF/polyoxometalate composites[22,23,26] and more recently organoclay MOF.[11] Although MOF-based composite modified electrodes exhibit excellent sensitivity and selectivity toward organic and inorganic targets,[16] the composite film on the electrode surface requires stabilization, which has mainly been achieved by using a conductive polymer such as Nafion.

In this work, we report on the solvothermal synthesis of an organoclay/Cu-MOF ($Cu_3(BTC)_2$) composite exhibiting the ability to form a stable film on glassy carbon electrode (GCE) without a polymer and further investigate the film GCE redox accessibility, electrochemical catalysis and electrochemical sensing activity toward three physiologically important compounds: deoxyepinephrine (DXEP), acetaminophen (AC) and tyrosine (TYR). Deoxyepinephrine or *N*-methyldopamine, is a derivative of catecholamine, which is present in insects and plants.[27] As a drug, DXEP is suitable for epinephrine substitution and is used to relieve high blood pressure, and for the treatment of cardiovascular arrest and congestive heart failure.[28] Acetaminophen or paracetamol (*N*-aminophenol) is a popular analgesic and antipyretic drug, of which an overdose can cause serious health complications.[29] Tyrosine (4-hydroxyphenylalanine) is an amino acid derivative of phenylalanine indispensable for maintainance of nitrogen (N) balance in humans. It is also a very important precursor for the synthesis of some catecholamines.[30] In biological fluids, acetaminophen often coexist and interfere with catecholamines.[31] For all these reasons, the monitoring of these three compounds is essential for the human wellbeing. Even if several successful methods for the quantification of these analytes are available,[32–34] electrochemical methods offer a most promising approach even though electrochemical determination of catecholamine, acetaminophen and tyrosine at bare conventional electrodes suffer from electrode fouling, slow electron transfer and interference of their electrochemical response.[35–37]

2. Experimental

2.1 Materials, chemicals and reagents

The natural clay, predominantly containing smectite, was collected from Sabga deposit (North West Cameroon in Central Africa) and its fine fraction was utilized to prepare the organoclay. The clay fine fraction (particles <2 μm) was obtained by the process of sedimentation of the pristine clay and then converted into its sodium form as reported elsewhere.[13] The homoionic fine fraction (namely Sa) was then collected as reported in the literature.[38] Copper(II) nitrate trihydrate ($Cu(NO_3)_2 \cdot 3H_2O$) (Abcr Chemical, 99.5%), trimesic acid (Sigma Aldrich, 98%), ethanol (Abcr Chemical, 99.8%)), *N*,*N*-dimethylformamide (DMF, Abcr Chemical, 99.8%), hydrochloric acid (HCl, Sigma Aldrich, 36.8–38%), deoxyepinephrine (DXEP, Abcr Chemical, 99%), acetaminophen (AC, Sigma, 98.%), tyrosine (TYR, Sigma, 98%), K_2HPO_4 (Sigma, 98%), KH_2PO_4 (Sigma, 98%), KCl (Synth Lab, 99%), CH_3COOH (Synth Lab, 99.8%), and CH_3COONa (Synth Lab, 99%) were purchased and used without any treatment.

2.2 Dye adsorption study and preparation of organoclay

The organoclay was prepared by absorbing thionin acetate dye into a natural Cameroonian, clay predominantly made of smectite, with surface area and cation exchange capacity (CEC) of 86 $m^2\ g^{-1}$ and 0.89 meq. g^{-1}, respectively.[39] Optimal conditions for the absorption of the dye by the clay were firstly determined. Experimentally, a known amount of sodium homoionic clay (fine fraction) was introduced into a 50 mL vial containing the thionin acetate dye (20.0 μM). The suspension was sonicated for 30 minutes and then magnetic stirred for a fixed time (1–60 min) after which it was allowed to attain exchange equilibrium. The solid was collected and the filtrate had no thionin dye according to spectrophotometry, which showed no characteristic absorption band at 600 nm.[40] The amount of dye adsorption was evaluated using eqn (1).

$$Q_e = \frac{(C_o - C_e)}{W} V \quad (1)$$

where C_o and C_e are initial and equilibrium concentrations of thionin dye expressed in mg L^{-1}, respectively. W (g) and V (L) are the mass of the clay sample and the volume of the dye solution, respectively.

The organoclay was prepared by intercalating the thionin acetate dye into a natural Cameroonian clay (Sa) interlayer space. 2.0 g of Sa was dispersed in 250.0 mL of dye (20.0 μM, pH 7) and stirred for 30 min. The solid organoclay, designated as Sa-TN, was collected by centrifugation and washed with distilled water and then dried in an oven at 50 °C.

2.3 Preparation of Cu-MOF and organocly/Cu-MOF composite

The copper MOF (Cu_3 $(BTC)_2$) was synthesized following a solvothermal method, as previously reported[41] but with slight modification. In this case, 1 mmole of $Cu(NO_3)_2 \cdot 3H_2O$ and 0.67 mmoles of trimesic acid were dissolved in a solvent mixture made of DMF (12 mL), ethanol (8 mL) and water (10 mL). The obtained solution was transferred into a 50 mL PTFE Teflon lined autoclave and thoroughly mixed for 10 min and then heated in an oven for 17 h at 80 °C. After cooling to room temperature, the resulting suspension was filtered and the resulting blue material was thoroughly washed with DMF/Ethanol/water mixture before being dried for 24 hours at 80 °C[42,43] to yield a blue colored powder.

The organoclay MOF composite was synthesized following a solvothermal method. Typically, a solvent mixture containing Cu-MOF precursors (*i.e.*, that which is used to prepare the pristine MOF) was added slowly to a PTFE Teflon lined autoclave containing well dispersed organoclay suspension, which was prepared by suspending a given amount of organoclay in ethanol/water (2/3) solvent mixture under stirring. The mixture was then heated in an oven at 80 °C for 17 h. The amount of organoclay was varied from nil to 50% while the composition of MOF precursor was kept constant, and the obtained composite was denoted Sa-TN_x/Cu-BTC (x is the mass percentage of organoclay added *i.e.* 5% for Sa-TN_5/$Cu_3(BTC)_2$, 10% for Sa-TN_{10}/$Cu_3(BTC)_2$, 25% for Sa-TN_{25}/$Cu_3(BTC)_2$ and 50% for Sa-TN_{50}/$Cu_3(BTC)_2$).

2.4 Preparation of the working electrodes

The working electrode was made using glassy carbon (GCE, $Ø$ = 2 mm) as substrate. Prior to its utilization and modification, the bare glassy carbon was polished to a mirror like surface with three different sizes of alumina (1, 0.3 and 0.05 μm) suspension slurry on individual polishing pad, followed by thorough rinsing with distilled water and sonication in a 1 : 1 mixture of ethanol and water. Modification of the glassy carbon was achieved by depositing some microliters of the suspension of composite prepared in DMF onto the electrode surface. The coating was left to dry for 4 h at room temperature. The obtained electrode was denoted Sa/GCE, Sa-TN/GCE, Sa-TN/$Cu_3(BTC)_2$/GCE when the modifier suspension was made of pristine clay (Sa), organoclay (Sa-TN) and the composite (Sa-TN/$Cu_3(BTC)_2$), respectively.

2.5 Instrumentation

Fourier transform infrared (FTIR) spectra of pristine samples and composites were recorded using an attenuated total reflection FT-IR spectrophotometer (Bruker Alpha – T-Spectrophotometer). Powder X-ray diffraction (XRD) analyses were performed with a Bruker X-ray diffractometer D8-Advance with Cu-Kα radiation. Scanning electron microscopy (SEM) coupled with energy dispersed spectroscopy (EDS) analyses were performed with Auriga SEM. A micromeritics sorptometer was used to determine the surface area and porosity from nitrogen adsorption–desorption isotherms obtained at 77 K. μ-Autolab Potentiostat (PGSTAT 12) controlled by GPES software was used for electrochemistry experiments in aerobic condition in three electrodes cell: glassy carbon electrode (GCE) as solid substrate for working electrode, saturated calomel electrode (SCE) as reference electrode and platinum wire as counter electrode. Differential pulse voltammetry (DPV) was carried out in the potential interval ranging from 0 to 0.9 V with scan rate of 50 mV s^{-1} (modulation amplitude of 0.04995 V, step potential of 0.00495 V, modulation time of 0.05 s and interval time of 0.1 s).

3. Results and discussion

3.1 Kinetic study of the adsorption of thionin by Sa clay

The adsorption kinetics of the thionin dye onto clay fine fraction (Sa) are shown in Fig. S1.† As observed an adsorption rate was achieved in the first 7 min., and equilibrium was achieved within 30 min. The adsorption kinetic study of TN by clay is better fitted for a pseudo second order model (R^2 = 0.9999) (Fig. S1B†), indicating that the adsorption process of TN by Sa likely involved chemical interactions.[44] The adsorption isotherm of TN by Sa is presented in Fig. S1C.† As revealed by Fig. S1D and data in Table S1,† the equilibrium data fitted the Langmuir model better. These results suggest that the adsorption of the dye occurs as monolayer onto clay surface. At pH 7, the clay shows high adsorption capacity (1.99 μmol g^{-1}), given that at this pH the clay is negatively charged thus, it will interact electrostatically with the cationic dye.[45]

3.2 Physicochemical properties of organoclay and organoclay Cu-MOF composite

The homoionic clay and organoclay were characterized by XRD and their patterns are shown in Fig. 1A. As shown on both diffraction patterns of pristine clay (pattern a) and modified clay (pattern b), the d_{001} peak is located at 2θ of 8.12° and 6.79°, respectively. This finding indicates that the interlayer space of the pristine clay has expanded from 11.56 to 13.13 Å, *i.e.* by *ca.* 1.56 Å, indicating that the dye was located in the interlayer space. The expansion indicated that the cationic dye intercalated into clay with the plane of its carbon parallel to the clay sheet plane, given that the cationic thionin dye is a flat molecule of size 7.2 × 15 Å on the basis of van der Waals radii.[2]

Fig. 1B shows the FT-IR spectrum of pristine clay before (Fig. 1B, spectra a) and after the intercalation of the dye into its interlayer (Fig. 1B, spectra b). For the pristine clay (curve *a*), the –OH stretching vibration band was observed at 3627 cm^{-1},

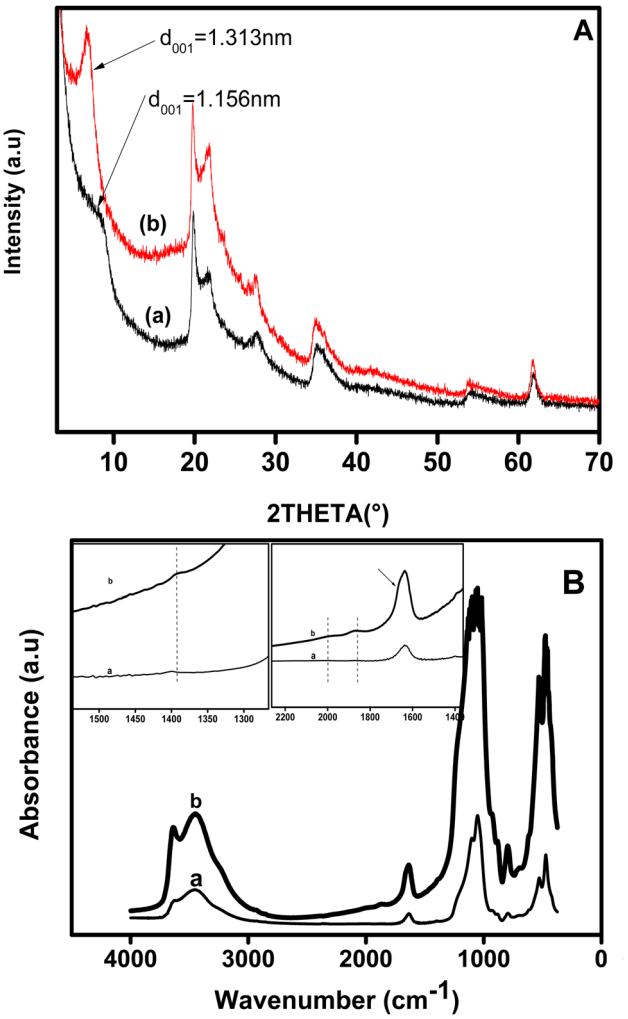

Fig. 1 (A) XRD patterns of pristine clay (plot a) and organoclay (plot b) and (B) FT-IR spectrum in KBr of pristine clay (spectra a) and dye intercalated clay (spectra b). The insets show magnification of the regions 1350–2250 cm^{-1} and 1225–1550 cm^{-1}.

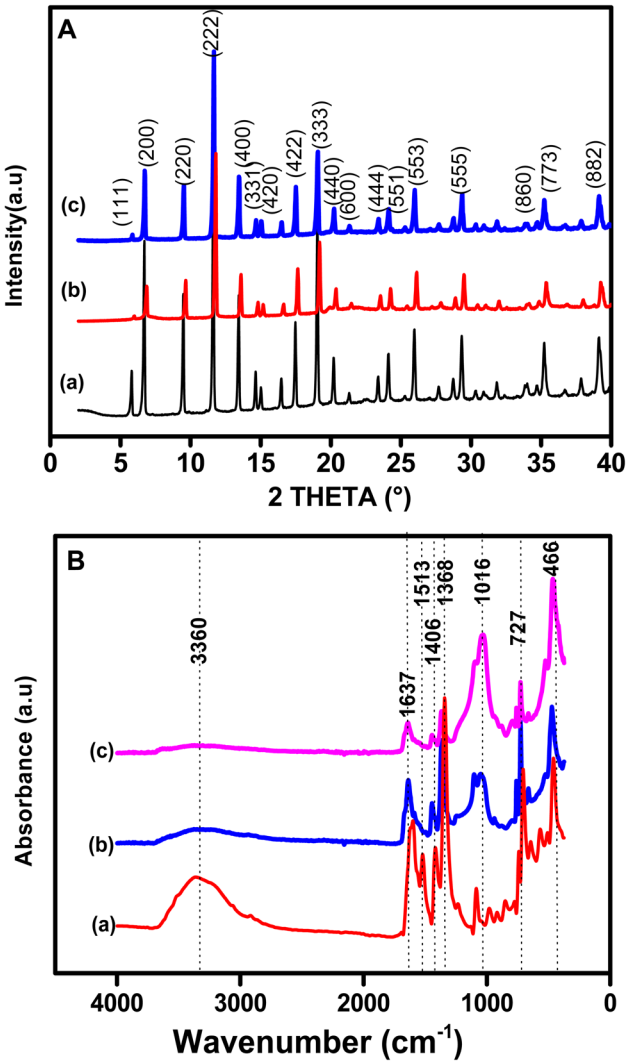

Fig. 2 (A) XRD patterns and (B) FT-IR spectra of (a) $Cu_3(BTC)_2$, (b) Sa-$TN_5/Cu_3(BTC)_2$ and (c) Sa-$TN_{50}/Cu_3(BTC)_2$.

while bands at 3460 and 1630 cm^{-1} were attributed to the bending mode vibration of absorbed water. The broad band at 1050 cm^{-1} was ascribed to the asymmetric stretching vibration of Si–O in the Si–O–Si group, and shifted to 1060 cm^{-1} for the organoclay (curve *b*). The band at *ca* 1600 cm^{-1} on the spectrum of dye intercalated clay showed a little shoulder 1660 cm^{-1} attributed to the N–H bending mode of the dye. Two weak bands that appeared at 1869 and 2038 cm^{-1} in curve *b* and were absent in spectrum a, may be assigned to the overtone band of the aromatic. The band occurring at 1393 cm^{-1} for organoclay was attributed to the C=C skeleton stretching.

Fig. 2A presents the XRD patterns of pristine Cu-MOF (pattern a) and organoclay/Cu-MOF composites (patterns b and c) prepared with different amounts of organoclay. The patterns show narrow and intense peaks, indicating good crystallinity for the as-synthesized products. The XRD pattern of the pristine MOF shows characteristic peaks of Cu-MOF at $2\theta =$ 5.6°, 6.7°, 9.5°, 11.6°, 13.5°, 17.5°,19.0° and 25.8°. The as-synthesised material contained CuO and Cu_2O as revealed by the characteristic XRD peaks at $2\theta = 35.5°$ and 38.7° for the first copper oxide and 36.4° for the second.[46,47] The patterns of the as-synthesized composites, Sa-$TN_{10}/Cu_3(BTC)_2$ (curve *b*), and Sa-$TN_{50}/Cu_3(BTC)_2$ (curve *c*), exhibited the same characteristic diffraction peaks as the pristine MOF, indicating that these composites featured the typical Cu organic framework and, secondly, that the embedment of the Cu-MOF with the organoclay did not modify the well-known structure of Cu-MOF. In addition, the organoclay composites exhibited sharp peaks similar to those of the pristine MOF, indicating that the MOF within the composites was crystalline. However, the intensities of these peaks for the composite became weaker as the organoclay content increased, revealing that high content of the organoclay in the starting mixture containing MOF precursors had an impact on the formation of the Cu-MOF crystals, and thus a less ordered crystalline structure was formed in the hybrid material. These observations also indicate that loading of an appropriate amount of organoclay is required to maintain the crystallinity as well as the octahedral shape of the MOF.

The FTIR spectrum of pristine Cu-MOF (curve *a*) and those of various composites are shown in Fig. 2B (curve *b* for Sa-TN_{10}/$Cu_3(BTC)_2$ and curve *c* for Sa-TN_{50}/$Cu_3(BTC)_2$). For spectrum (a), the characteristic vibration bands of Cu-BTC can be observed, namely, at 1642 and 1513 cm^{-1}, corresponding to the asymmetric stretching modes (1642 cm^{-1} is the aromatic C=C and 1513 cm^{-1} from C=O of H_3BTC),[48] and at 1406 cm^{-1} and 1368 cm^{-1} arising from symmetric stretching modes (1406 cm^{-1} due to C=O and 1368 cm^{-1} from C–O of H_3BTC).[48] The band at 1060 cm^{-1} can be assigned to the C–H vibration of the aromatic ring. In addition the vibration at 725 cm^{-1} is likely a Cu–O stretching vibration due to the coordination of the oxygen atom to Cu^{2+}. The bands at 630 cm^{-1}, 550 cm^{-1} and 460 cm^{-1} can be related to CuO and Cu_2O. The characteristic bands of the Cu-MOF are generally present in the spectra of the various composites as shown in Fig. 2B (spectra b and c). Moreover, comparison of the FTIR spectrum of the composites shows that there is a good agreement in terms of position and intensity of the characteristic bands of Cu-MOF. These findings are consistent with the fact that the introduction of appropriate amounts of organoclay did not interfere with the structure of the Cu-MOF. The only significant difference between the spectrum of the composites and that of the pristine MOF is the broad band for curve *a* at 3000–3800 cm^{-1}, ascribed to stretching of hydrogen-bonded O–H group and the intense band at 1500 cm^{-1} attributed to Si–O–Si. The EDS analysis of the Sa-TN_{10}/$Cu_3(BTC)_2$ composite confirmed the presence Si and Al together with C, O and interestingly Cu, thus demonstrating that the composite was likely made of clay interconnected to the Cu-MOF (Fig. S2†). The average crystallite sizes of the pristine MOF and the composites were calculated using the Scherrer equation:

$$d = \frac{k\lambda}{\beta \cos \theta} \quad (2)$$

where β represents the FWHM (Full Width at Half Minimum) measured in radian on 2θ and θ is the Bragg angle for diffraction peaks, λ is the wavelength of X-rays, d is the crystallite size and k is a constant (0.9). The crystallite size of Cu-MOF was estimated to be *ca.* 25 nm, close to that reported in the literature.[49] In the presence of the organoclay, the crystallite size of Cu-MOF within the composites was between 55 and 58 nm. The increase in Cu-MOF crystallite size in the composite compared with that of pristine MOF implied a correlation between the amount of organoclay added to MOF precursors solution and the crystallite size of Cu-MOF indicating that high amount of organoclay led to larger crystallite size.

The SEM images of the Cu-BTC MOF, clay and Sa-TN/$Cu_3(BTC)_2$ composites are shown in Fig. 3. In the SEM images of

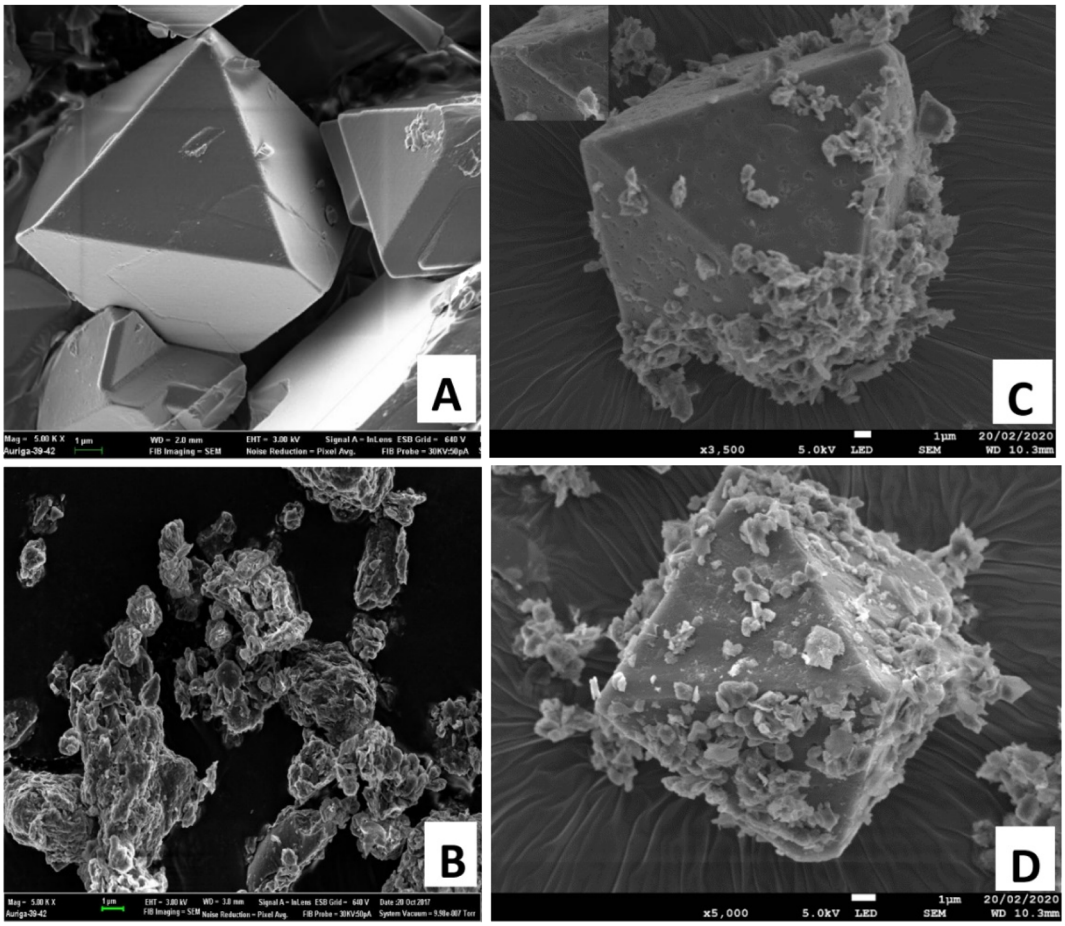

Fig. 3 SEM images of pristine $Cu_3(BTC)_2$ (A), organoclay (B), Sa-TN_{25}/Cu3$(BTC)_2$ (C) and Sa-TN_{50}/Cu3$(BTC)_2$ (D).

the pristine MOF (Fig. 3A), it can clearly be seen that $Cu_3(BTC)_2$ particles are well-formed with a truncated octahedral geometry, which is in agreement with their XRD patterns. Their average edge to edge length was estimated to be between 10–12 μm. The image of organoclay (Fig. 3B) depicts a compiled platy morphology characteristic of smectite clay minerals. The SEM image of composites Sa-TN_{10}/Cu-BTC (Fig. 3C) and Sa-TN_{50}/Cu-BTC (Fig. 3D) shows the clay sheets and the typical truncated octahedral structure of Cu-MOF, the crystal being covered by organoclay leading to a rough surface as observed in Fig. 3C and D. The presence of the organoclay on the surface of the MOF acts to prevent the aggregation between crystals and favor the formation of a stable film at the electrode substrate.

Fig. 4b shows the N_2 adsorption–desorption isotherms of pristine Cu-MOF (plot a) and the composites (plot b for Sa-TN_{10}/$Cu_3(BTC)_2$, plot c for Sa-TN_{50}/$Cu_3(BTC)_2$ and the pristine clay (plot d). A type IV isotherm was obtained with the pristine MOF and Sa-TN_{10}/$Cu_3(BTC)_2$, highlighting their microporosity, while that of clay was type IV with a H3 hysteresis loop attributed to the layer structure of the clay. Interestingly Sa-TN_{50}/$Cu_3(BTC)_2$ composites exhibited type IV isotherm along with a small hysteresis loop at high relative pressure, which indicates the presence macro- and mesopores associated with the interparticle spaces[50] in the composite. The surface area of the pristine Cu-MOF was 1408 $m^2\ g^{-1}$, close to the value reported elsewhere in the literature for bulk Cu-MOF.[51] The surface area of the composites was 569 $m^2\ g^{-1}$ for Sa-TN_{10}/$Cu_3(BTC)_2$, and 192 $m^2\ g^{-1}$ for Sa-TN_{50}/$Cu_3(BTC)_2$. The reduced surface area of the composites is likely due to the low porosity nature of organoclay (91 $m^2\ g^{-1}$, curve *d*, Fig. 4) covering the MOF surface. The detail data of pore volume of the pristine MOF, pristine clay and clay MOF composites are presented in Table 1.

3.3 Electrochemical behavior of DXEP, AC and TYR on Sa-TN/Cu-BTC/GCE

As reported in the literature, deoxyepinephrine (DXEP) and acetaminophen (AC) undergo multistep reactions

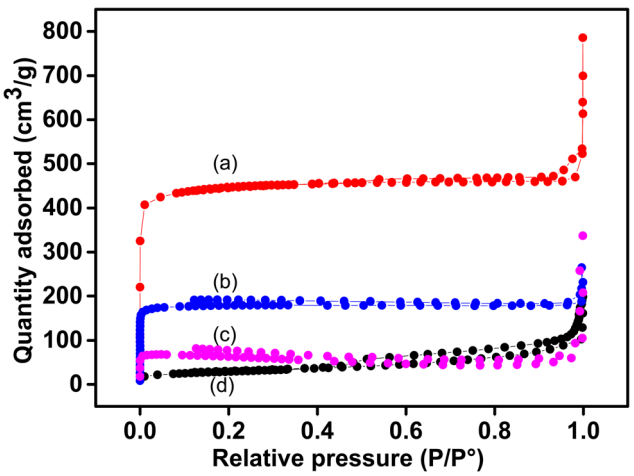

Fig. 4 N_2 isotherms of pristine $Cu_3(BTC)_2$ (a) and those of composites: Sa-TN_{10}/Cu3(BTC)$_2$ (b), Sa-TN_{50}/$Cu_3(BTC)_2$ (c) and pristine clay (d).

Table 1 Textural properties of pristine Cu_3 $(BTC)_2$, clay and their composites

Materials	BET surface area ($m^2\ g^{-1}$)	Micropore volume ($cm^3\ g^{-1}$)	Micropore size (nm)
Cu_3 $(BTC)_2$	1408	0.70	0.57
Sa-TN_{10}/$Cu_3(BTC)_2$	569	0.28	0.31
Sa-TN_{50}/$Cu_3(BTC)_2$	192	0.09	0.30
Sa	91	0.05	0.86

corresponding to Electrochemical-Chemical-Electrochemical (ECE) (Scheme 1A) and Electrochemical-Chemical (EC) (Scheme 1B) mechanisms. As catecholamine, DXEP in aqueous media undergoes a first two-electron oxidation process leading to a catecholamine *o*-quinone, which can then result in a cyclisation and yield leucoaminochrome. Leucoaminochrome is easily oxidisable by exchanging two electrons to form aminochrome.[8] In the EC mechanism of AC, its two-electron oxidation leads to *N*-acetyl-*p*-benzoquinone imine and after chemical reaction it is transformed to *p*-benzoquinone.

Cyclic voltammetry (CV) was employed to investigate the electrochemical behavior of the three analytes individually in acetate buffer (AcB) pH 5 at bare GCE, pristine clay film electrode (Sa-GCE) and composite modified electrode (Sa-TN/$Cu_3(BTC)_2$/GCE). Fig. 5 shows CVs recorded at 50 mV s^{-1} in AcB containing either 138 μM DXEP (Fig. 5A) or 154 μM AC (Fig. 5B) at bare GCE (curve *a*), Sa/GCE (curve *b*) and Sa-TN_{50}/$Cu_3(BTC)_2$/GCE (curve *c*). As shown in Fig. 5A, when the electrolyte solution contained the catecholamine and the potential scan was run in the positive direction, a well-defined peak appeared. However, in the reverse potential scan, no peak appeared within the potential range examined. This reveals that the electrochemical process is irreversible. This behavior can be rationalized by the fact that the dopamichrome can undergo polymerisation reaction on GCE electrode surface leading to the fouling of the electrode. Interestingly, contrary to CV recorded at bare electrode, those recorded in the same conditions at Sa/GCE and Sa-TN_{50}/$Cu_3(BTC)_2$/GCE exhibited a pair of redox peak centered at $E_{1/2} = +0.26$ V and $E_{1/2} = +0.17$ V, respectively, besides the peak current ratio I_{pa}/I_{pc} was different from unity, corroborating the quasi-reversible nature of the electrochemical reaction of DXEP at the modified electrodes. These results show complementarity between the clay and MOF. Indeed, the quasi-reversible process observed at the modified electrode may be due to the fact that at pH 5 the DXEP and its electrooxidation products are positively charged, favoring the electrostatic attraction between the negatively charged clay sheet and these products. Moreover, the intracyclization of the protonated product of the oxidation of DXEP cannot take place under acidic condition, but the amine group was being transformed to ammonium, thus resulting in less electrode fouling. In addition, the amino or hydroxy group of the three analytes can undergo van der Waals/electrostatic interactions with silanol groups on the clay surface, favoring their diffusion through the film at the electrode surface. Although the CVs recorded at modified electrode exhibited a quasi-reversible process, the current ratio, I_{pc}/I_{pa}, was *ca* 0.6

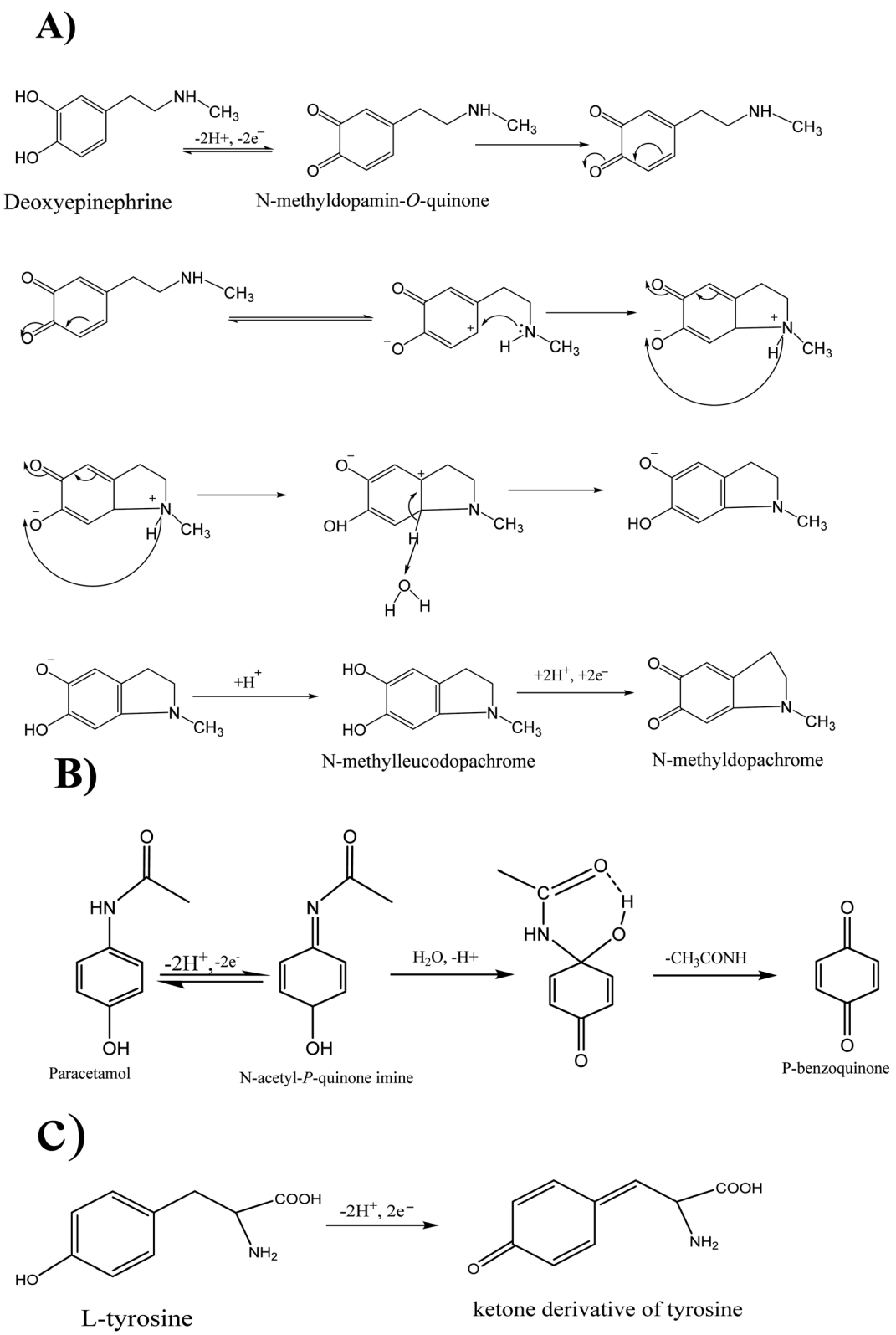

Scheme 1 Reaction mechanism of (A) DXEP,[55] (B) AC[56] and (C) TYR.[57]

for Sa-TN_{50}/$Cu_3(BTC)_2$/GCE and *ca* 0.2 for Sa/GCE. The anodic and cathodic potential separation at CV recorded at Sa/GCE was found to be 0.61 V, three times higher than that obtained at Sa-TN_{50}/$Cu_3(BTC)_2$/GCE. The increase in reversibility associated to the negative shift of the oxidation potential and the positive shift in reduction potential of DXEP in addition to peaks current increase, suggests that the MOF within the film onto the electrode surface likely catalyzed the oxidation of DXEP. This may

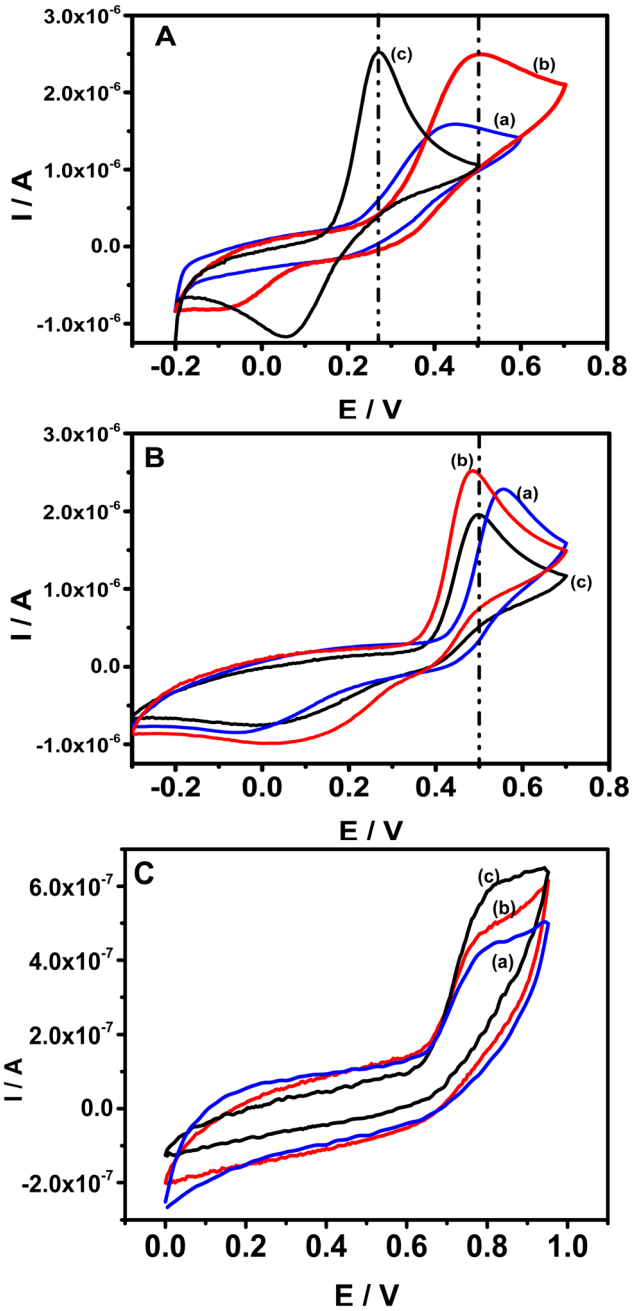

Fig. 5 CVs recorded at bare GCE (a), Sa (b) and SaTN$_{50}$/Cu$_3$(BTC)2/GCE (c) in 0.1 M AcB (pH 5.0) containing either: (A) 138.0 μM of DXEP, (B) 154.0 μM of AC or (C) 44.2 μM of TYR. Scan rate 50 mV s^{-1}.

have occurred through the intermediary of an adduct formed between the oxidized product of DXEP and the MOF.

When the electrolyte solution contained AC, although CVs recorded at bare GCE exhibited an anodic and a cathodic peak (see Fig. 5B), the anodic peak was positively shifted whereas the cathodic peak was negatively shifted compared with the corresponding CVs recorded at modified electrode, with a larger peak to peak separation ΔE estimated to be 0.54 V and $I_{pc}/I_{pa} \approx 0.2$. This ΔE value is 10 mV higher than that obtained at Sa/GCE, which exhibited a current ratio of *ca.* 0.45, suggesting that as for DXEP, the presence of clay film onto the electrode surface favored the redox reaction of positively charged AC. Interestingly, although the redox potentials recorded at Sa-TN$_{50}$/Cu$_3$(BTC)$_2$/GCE are aligned with those of Sa/GCE, the electrochemical response of the AC oxidation at Sa-TN$_{50}$/Cu$_3$(BTC)$_2$/GCE was slightly lower than that recorded at Sa/GCE. These observations suggest that Cu-MOF does not have catalytic effect on the oxidation of AC contrary to what was observed with DXEP. It is worthy to note that the oxidation peak potential corresponding to the oxidation of AC at Sa/GCE appeared nearly at the same potential as the oxidation of DXEP, resulting in an overlap of their voltammetry response, as for bare glassy carbon, while at Sa-TN$_{50}$/Cu$_3$(BTC)$_2$/GCE these corresponding peak potentials are well separated.

In the presence of TYR as shown in Fig. 5C, when the potential was scanned in the positive direction, an oxidation peak appeared at +0.78 V at TN$_{50}$/Cu$_3$(BTC)$_2$/GCE (curve *c*), and +0.81 V at Sa–Sa/GCE (curve *b*) and GCE (curve *a*). Meanwhile in the reverse potential scan, as expected no peak was observed, indicating that at modified and unmodified electrodes, the electrochemical process of TYR is an irreversible process. The enhancement of the current at modified electrodes is likely due to the fact that this analyte, as do DXEP and AC, can diffuse through the negatively charged film onto the electrode surface through van der Waals/electrostatic interactions with silanol group on the clay surface.

Fig. 6 compares the differential pulse voltammograms (DPV) recorded at bare GCE and composite electrodes (Sa-TN$_{50}$/Cu$_3$(BTC)$_2$/GCE) in AcB (pH 5) containing the mixture of DXEP, AC and TYR. As expected from the CV results of Fig. 5, the voltammogram recorded at the composite modified electrode shows three well-defined oxidation peaks at +0.20 V, +0.42 V and +0.72 V, attributed, respectively, to the electro-oxidation of DXEP, AC and TYR. At the bare GCE, two well resolved peaks appear at +0.48 V and 0.74 V attributable to the electro-oxidation of AC and TYR, respectively, the first peak being overlapped by dome due to the oxidation of DXEP. This result is consistent with the CV response, confirming that the electrochemical response of AC at bare GCE interfered with that of DXEP as

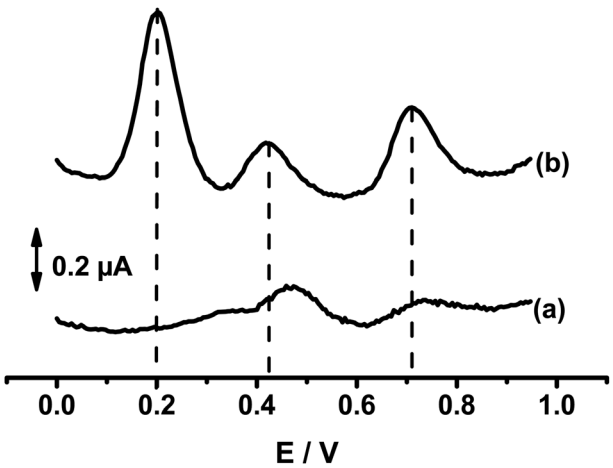

Fig. 6 DPVs recorded at bare GCE (a) and SaTN$_{50}$/Cu$_3$(BTC)2/GCE (b) in 0.1 M AcB (pH 5) containing 19.8 μM of DXEP, 23.8 μM of AC and 44.2 μM of TYR.

reported in the literature.[52–54] The peak-to-peak separations at Sa-$TN_{50}/Cu_3(BTC)_2$/GCE were found to be $\Delta E_{DXEP\text{-}AC}$ = 22 mV and $\Delta E_{DXEP\text{-}TYR}$ = 27 mV. Thus at modified electrode the simultaneous detection of the three analytes is feasible.

The electrochemical response of glassy carbon modified with different composites, namely, (Sa-$TN_5/Cu_3(BTC)_2$, 5% for Sa-$TN_{10}/Cu_3(BTC)_2$, 25% for Sa-$TN_{25}/Cu_3(BTC)_2$ and 50% for Sa-$TN_{50}/Cu_3(BTC)_2$) modified GCE were examined under the same conditions of pH and electrolyte solution containing 19.8 μM of DXEP, 23.8 μM AC and 44.2 μM TYR. It was found (Fig. S3†) that at the composite modified electrode Sa-$TN_{50}/Cu_3(BTC)_2$, three well-defined oxidation peaks appeared on sweep voltammograms corresponding to the oxidation of DXEP, AC and TRR, while at the other composite film electrodes, only the oxidation peak of DXEP and AC were observed. In addition, the Sa-$TN_{50}/Cu_3(BTC)_2$ modified electrode demonstrated better sensitivity associated with a negatively shifted potential mainly for DXEP and AC, in comparison with electrochemical response recorded at Sa-$TN_5/Cu_3(BTC)_2$, Sa-$TN_{10}/Cu_3(BTC)_2$ and Sa-$TN_{25}/Cu_3(BTC)_2$. These results also demonstrate the synergistic effect of the MOF and organoclay, which can be explained by the good crystallinity of $Cu_3(BTC)_2$ within the composite film at Sa-$TN_{50}/Cu_3(BTC)_2$ and its stability, with the organoclay forming an interconnected network which may favor charge transfer as well as the stability of the film at the electrode surface. For these reasons, Sa-$TN_{50}/Cu_3(BTC)_2$ modified glassy carbon electrodes were further explored as sensors.

To investigate the electrochemical reaction kinetics at Sa-$TN_{50}/Cu_3(BTC)_2$/GCE, the effect of scan rate was studied (Fig. 7). For the three analytes, the electrochemical response increased with the scan rate and the oxidation peak potentials were positively shifted while the reduction peak potentials were negatively shifted. Although the redox peak potential shifted with the increase of the scan rate, their potential difference remained nearly constant (≈200 mV for DXEP (Fig. 7A) and 400 mV for AC (Fig. 7B)). The insets of Fig. 7 show that for all analytes, the plot of current peak *versus* the square root of the scan rate ($v^{1/2}$) resulted in a straight line. This linearity suggests that the electrochemical reaction of the three analytes at Sa-$TN_{50}/Cu_3(BTC)_2$/GCE is an apparent diffusion controlled process. The plot of log of the oxidation current *versus* log of scan rate was also obtained and were found to be linear with the slope of 0.6 ($R^2 = 0.996$), 0.4 ($R^2 = 0.995$) and 0.5 ($R^2 = 0.996$) for DXEP, AC and TYR, respectively. These values are not far from 0.5, which confirms that the electro-oxidation of these analytes at Sa-TN/$Cu_3(BTC)_2$/GCE is predominantly controlled by an apparent diffusion[10] and that the electrode was not fouled by these analytes and/or the product of the reaction.

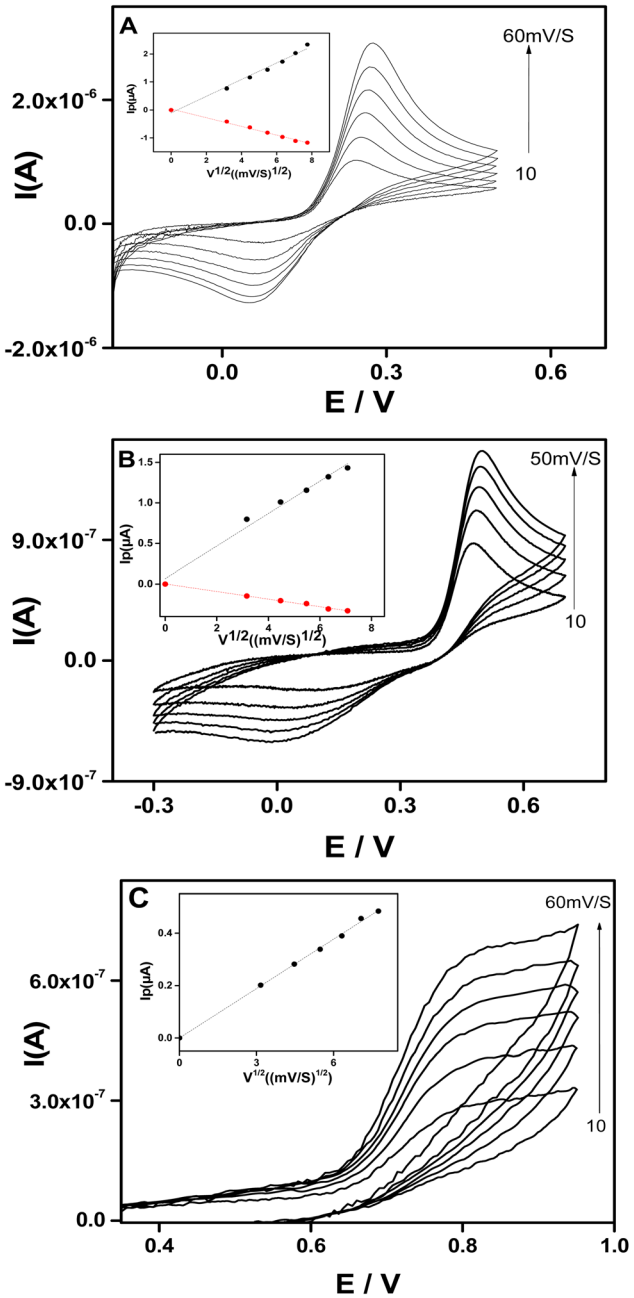

Fig. 7 CVs recorded at different scan rates at Sa-$TN_{50}/Cu_3(BTC)_2$/GCE in AcB pH 5.0 containing either: (A) 138.0 μM DXEP, (B) 154.0 μM AC or (C) 44.2 μM TYR. Insets show the linear relationship between the peak current *vs.* square root of the scan rate ($v^{1/2}$) and log *E vs.* log *v*.

3.4 Optimization of the experimental parameters

The estimation of the optimal experimental parameters were achieved using Sa-$TN_{50}/Cu_3(BTC)_2$/GCE.

3.4.1 Effect of the amount Sa-$TN_{50}/Cu_3(BTC)_2$ onto GCE surface. The sensitivity of the modified electrode is usually affected by the film thickness, which can be tuned by varying the amount of the modifier. We probed the dependence of oxidation peak current of DXEP, AC and TYR on the amount of the composite (4.0 to 20.0 mg) dispersed in 2.0 mL of DMF and from which 2.0 μL was taken and dropped onto GCE and left to dry at room temperature. We found that (Fig. S4†) the electrochemical response for the three analytes increased then leveled off when the suspension was prepared by dispersing 4 mg of composite in DMF. The peak current then decreased due to the fact that the modification film on GCE was very thick with organoclay, which caused electrical resistance for the analytes. Thus the modification of the working electrode for further work

was made by drop casting 2.0 μL of the composite suspension (4.0 mg mL^{-1}) onto the electrode surface.

3.4.2 Effect of the pH of the electrolytic solution

The oxidation peak potentials as well as the electrochemical responses of DXEP (pK_a = 9.27 & 10.29), AC (pK_a = 9.5) and TYR (pK_a = 9.76) at Sa-TN_{50}/$Cu_3(BTC)_2$/GCE were found to vary with the pH of the buffer solution, indicating that the electrochemical behavior of these analytes was affected by the acidity of the electrolyte solution. This behavior was examined in buffer solution with pH ranging from 3.5 to 7.0 and containing simultaneously 18.0 μM DXEP, 14.0 μM AC and 24.0 μM Tyr. As can be observed in Fig. 8 and inset A, in the pH range from 3.0 to 7.0, the peak current was also found to augment from 3.0 to 5.0 then diminish before increasing again reaching the maximum current at pH 6 and then leveling off. Although the current was greater at pH 6 for DXEP and AC, the oxidation peak current as a result of TYR oxidation was very low. Thus, pH = 5.0 acetate buffer (shortened as AcB) where the electrochemical response vis-a-vis the three analytes were maximum, was chosen for further experiments. Interestingly, it was noted that for the three analytes, the oxidation peak potentials were negatively shifted as the electrolyte solution pH increased (Fig. 8A), revealing that protons were involved in the electrochemical reaction.[35] The inset B of the Fig. 8 shows that the oxidation peak potential and the electrolyte pH are linearly dependent with slope value of 79.1 (R^2 = 0.992) for DXEP, 42.98 (R^2 = 0.912) for AC and 61.5 (R^2 = 0.966) for TYR. All these values are close to the theoretical Nernstian value of 59.0 mV at 25 °C, suggesting that protons are involved in the electrochemical reaction process at the modified electrode as indicated in the following mechanisms in Scheme 1.

3.5 Determination of DXEP, AC and TYR at Sa-TN_{50}/$Cu_3(BTC)_2$/GCE

Under the optimal conditions the individual and simultaneous determination of DXEP, AC and TYR were investigated at Sa-TN_{50}/$Cu_3(BTC)_2$/GCE using DPV.

3.5.1 Individual determination of DXEP, AC and TYR. The individual determination of DXEP, AC and TYR was achieved by increasing the amount of one of these analytes in the electrolyte solution (AcB pH 5). The electrochemical response recorded at Sa-TN/$Cu_3(BTC)_2$/GCE is shown in Fig. 9A for DXEP; Fig. 9B for AC and Fig. 9C for TYR. In all cases, the peak currents ascribed to the oxidation of DXEP at ≈ +0.20 V, AC at +0.44 V and TYR at ≈ +0.76 V were observed to increase with the successive addition of a constant amount of the targeted analyte. As shown in the insets of Fig. 9A and B, the increase of electrochemical responses for the three analytes, taken individually, fit a linear equation within the concentration range 1.0–138.0 μM (R^2 = 0.995) for DXEP, 4–154.3 μM for AC (R^2 = 0.999) and 1.0–29.3 μM (R^2 = 0.993) for TYR. The sensitivities of the Sa-TN_{50}/$Cu_3(BTC)_2$/GCE were deduced from the slopes of the regression equation to be 0.024 μA $μM^{-1}$, 0.010 μA $μM^{-1}$ and 0.006 μA $μM^{-1}$ for DXEP, AC and TYR, respectively.

3.5.2 Simultaneous determination of DXEP, AC and TYR. The simultaneous determination of DXEP, AC and TYR was conducted by increasing the concentration of one analyte in the electrolyte solution containing a fixed concentration of the

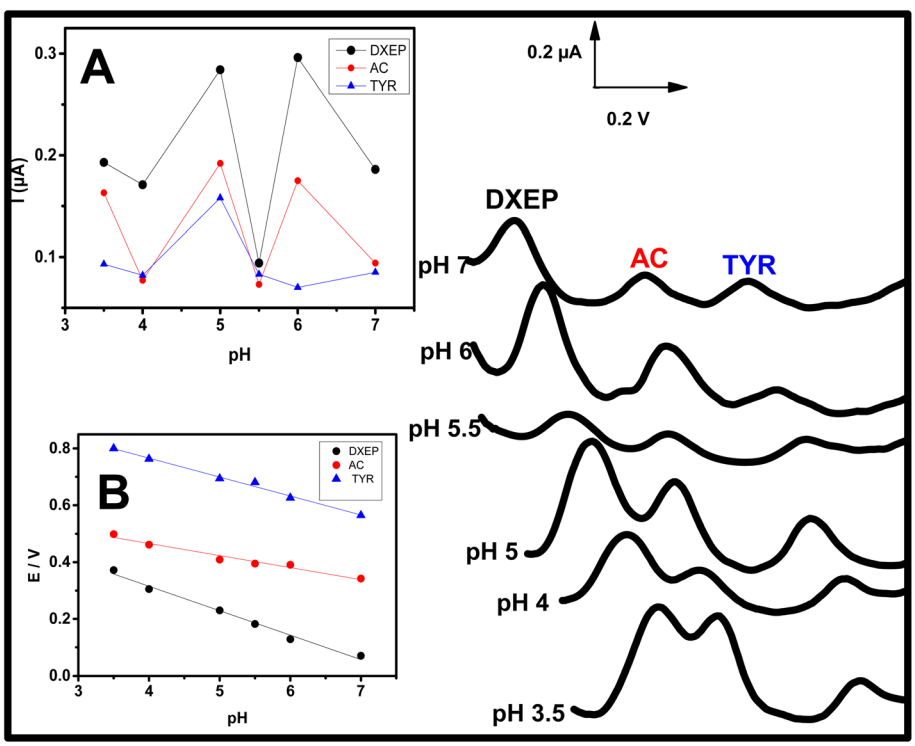

Fig. 8 (A) DPVs recorded at Sa-TN_{50}/$Cu_3(BTC)_2$/GCE at different buffers with pH ranging from 3.0 to 7.0 containing the three analytes mixture (19.8 μM DXEP, 23.8 μM AC and 44.2 Mm TYR). (B) Dependence of different oxidation peak potentials on pH.

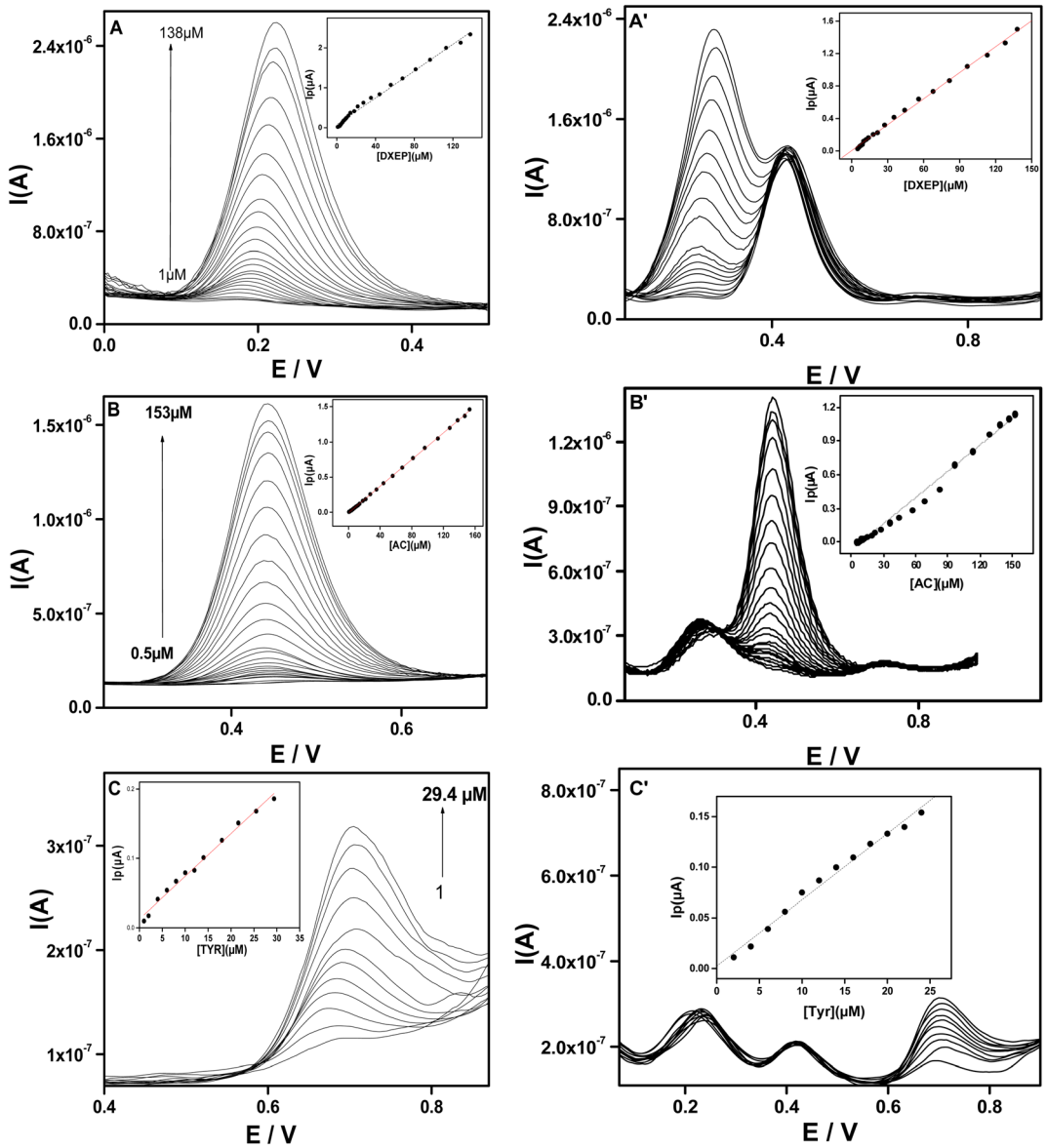

Fig. 9 DPVs recorded at Sa-TN_{50}/$Cu_3(BTC)_2$/GCE when successive addition of either (A) DXEP, (B) AC or (C) TYR were added in AcB buffer solution (pH = 5.0). DPVs recorded at Sa-TN_{50}/$Cu_3(BTC)_2$/GCE when successive addition of either of (A′) DXEP in AcB containing 153.0 μM AC and 17.3 μM TYR, (B′) AC in AcB containing 12.0 μM DXEP and 17.3 μM TYR or (C′) TYR in AcB containing 6.0 μM DXEP and 10.2 μM AC. Insets are corresponding calibration curves.

other two. As observed in Fig. 9A–C, when successive addition of DXEP was made in AcB (pH 5) containing a fixed concentration of AC (153.0 μM) and TYR (17.3 μM), the peak current associated with the oxidation of AC and TYR remained nearly constant while that of DXEP increased in line with increase in the concentration of DXEP. This increase of oxidation peak current due to DXEP depended linearly on the DXEP concentration ranging from 5.0 μM to 138.0 μM ($R^2 = 0.998$). Similarly, when AC was added gradually to the acetate buffer containing a constant concentration of 12.0 μM DXEP and 17.3 μM TYR, the electrochemical response as a result of the oxidation of AC was found to vary linearly with AC concentration from 4.0 to 154.3 μM. By keeping the concentration of DXEP (6.0 μM) and AC (10.2 μM) unchanged in the electrolyte solution, the oxidation peak current of TYR was also linearly dependent with its concentration ranging from 2.0 μM to 12.0 μM. The sensitivities of Sa-TN_{50}/Cu-BTC/GCE were, respectively, 0.016 μA μM^{-1}, 0.009 μA μM^{-1} and 0.007 μA μM^{-1}, for DXEP, AC and TYR. The detection limit estimated for each analyte was 0.4 μM for DXEP, 0.7 μM for AC and 0.2 μM for TYR. These results indicate that the performances of the developed sensors showed wider linear ranges as well as lower detection limits compared with other sensors reported in the literature (Table 2).

3.6 Interference study

The influence of inorganic (Ca^{2+}, Mg^{2+}, Zn^{2+} and Cu^{2+}) and organic (dopamine, uric acid, ascorbic acid and tryptophan)

Table 2 Comparison of the sensing performance of the developed sensors Sa-TN_{50}/Cu-BTC/GCE and those reported in literature[a]

Modified electrodes	Analytes	Linear range (μM)	Detection limit (μM)	Reference
CuFe2O4/1H3MBr/PE	DXEP	0.3–300	0.09	58
(CPE/CuO-NPs/HMIPF6		0.7–900	0.2	59
ZA/CPE		0.5–70	0.2	60
ZX/CPE		0.5–70	0.08	60
Sa-TN_{50}/Cu-BTC/GCE		**1–138**	**0.4**	**This work**
AuNPs/poly(trisamine)/GCE	AC	1.9–188	0.1	61
NiO/CNTs/DPID/CPE		0.8–550	0.3	62
CoTPyPRu(bipy)2–Ba/GCE		1–50	0.2	63
Au@Pd HNRs/BG/GCE		130–1010	6.35	64
poly-L-Asp/GPE		0.05–108.25	0.011	65
poly(Val)/CPE		5– 60	0.29	66
AuNPs/MWCNT/GCE		0.09–35.0	0.03	67
TCPP–Sa/CPE		1 – 90	0.2	68
HKUST-1/GCE		12.5–75	0.11	69
MWMOF-199/GCE		0.1–5	1.3	70
ZA/CPE		0.5–70	0.3	60
ZX/CPE		0.5–70	0.2	60
Sa-TN_{50}/Cu-BTC/GCE		**4–154.3**	**0.7**	**This work**
AuNPs/poly(trisamine)/GCE	TYR	3.9–61.8	0.9	61
NiO/CNTs/DPID/CPE		5.0–750.0	1	62
CoTPyPRu(bipy)2–Ba/GCE		1–25	0.5	63
Au@Pd HNRs/BG/GCE		30.00–360.00	3.71	64
poly-L-Asp/GPE		0.1–93.9	0.31	65
AuNPs/MWCNT/GCE		0.4–80	0.21	67
TCPP–Sa/CPE		3–51	0.7	68
Sa-TN_{50}/Cu-BTC/GCE		**1–21.6**	**0.2**	**This work**

[a] AuNP: gold nanoparticle, HNRs: hybrid nanorods; CPE: carbon paste electrode; HMIPF6: *n*-hexyl-3-methylimidazolium hexafluorophosphate H3MBr: 1-hexyl 1-3 methylimidazolium bromide; ZIF zeolitic imiazole framework; Val: valine; MWMOF: microwave organic framework; DPID: 2-(3,4-dihydroxyphenethyl) isoindoline-1,3-dione; H3MTFB: 1-hexyl 3-methylimidazolium tetrafluoroborate; L-Asp: L-aspartic acid, ZX: zeolite X; ZA: zeolite A; SPE: screen printed electrode.

interferences on the determination of DXEP, AC and TYR was evaluated by adding various species to the analyte mixture (5.0 μM DXEP + 5.0 μM AC + 5.0 μM TYR) in 0.1 AcB pH 5.0. In the presence of inorganic species, the electrochemical response toward DXEP, AC and TYR was not affected. When dopamine, ascorbic acid, uric acid or tryptophan were added at concentration lower than 2.0 μM in the electrolyte solution containing the three analytes, the response of the sensor toward these analytes was unaffected. However, for greater concentrations (*i.e.* >2 μM), the electrochemical response of DXEP was significantly affected by dopamine and that of AC was also affected by uric acid while the tryptophan interfered with the quantification of TYR.

3.7 Real sample analysis

Sa-TN/Cu-BTC/GCE was applied to estimate the AC content in a commercial tablet of Paracetamol 1000 mg (*i.e.* 1000 mg of AC/tablet) using the standard addition method. The tablet was finely ground in a mortar and the powder was then dissolved in water. The aqueous solution was centrifuged and 0.5 mL of the supernatant was transferred into an electrochemical cell containing 24.5 mL of AcB (pH 5) and DPV response was recorded (dashed line in Fig. S5†). Five successive additions of AC standard were then employed and the electrochemical response recorded each time (solid line in Fig. S5†). From the regression equation shown in the inset (Fig. S5†), the estimated amount of acetaminophen in the tablet was 96.75% of the theoretical amount AC of the paracetamol tablet. This result shows that the developed sensors can be used efficiently for AC quantification in real samples. The amount of the three targeted analytes in tap water was also determined using the same method. Experimentally, in order to perform real sample analysis of tap water, a known amount of DXEP, AC and TYR was spiked into the tap water. The sample was then added to the electrolytic solution so that the total volume of electrochemical cell was 10.0 mL. The DPVs were then recorded at the developed sensors. Five successive standards of the analytes were added to the solution and the DPVs recorded. The amount of each spiked sample obtained and recovery values are presented in Table S2.† For the three analytes the recovery value ranged from 90% to 102%, demonstrating the applicability of the developed sensors in real milieu.

3.8 Stability, repeatability and reproducibility of Sa-TN_{50}/$Cu_3(BTC)_2$/GCE

The results displayed in Fig. 9 show that the oxidation peak potentials obtained for simultaneous or individual detection of DXEP, AC and TYR are well correlated and show similar sensitivity. This confirms the good operational stability of the modified electrode toward the oxidation of the three analytes.

Since the electrode preparation is easy and rapid, it does not need to be stable for a long time. A repeatability study based on successive measurements of the electrochemical response using Sa-TN_{50}/$Cu_3(BTC)_2$/GCE prepared by drop coating of the composite suspension in the mixture of analytes in the electrolyte solution was carried out. The relative standard deviation (RSD) of seven successive measurements for the three analytes were estimated to be 1.5%, 1.2% and 1.4% for DXEP, AC and TYR, respectively, which indicate that Sa-TN/$Cu_3(BTC)_2$/GCE exhibited good repeatability and short term stability. The reproducibility of Sa-TN_{50}/$Cu_3(BTC)_2$/GCE was studied using five independent modified electrodes prepared similarly and used in electrolytic solution containing a mixture of analytes. RSD was 3.4%, 4.1% and 3.7% for DXEP; AC and TYR, respectively; which confirmed good reproducibility.

4. Conclusion

A copper MOF composite was prepared by growing the MOF crystals in a mixture containing MOF precursors and an organoclay. The organoclay was obtained by intercalating thionin dye into the interlayer of a natural Cameroonian clay. The characterization of the resulting blue crystal composite showed that it exhibited high surface area and appeared to be made of well-shaped hexagonal Cu-MOF crystals covered with clay. The composite film modified glassy carbon electrodes were fabricated by drop casting a suspension onto the electrode surface followed by drying at room temperature. The modified electrode demonstrated electrocatalytic activity vis-a-vis DXEP, thus allowing some selectivity of the modified electrode for the simultaneous determination of DXEP and AC, which was found to cause interference when using bare GCE. Thanks to the synergistic effect of organoclay and Cu-MOF at the surface of GCE, the composite modified glassy carbon electrode showed good selectivity and sensitivity for both the individual and simultaneous detection of DXEP, AC and TYR. The composite modified glassy carbon electrodes were successfully applied in the quantification of AC in a commercial tablet and the three analytes (DXEP, AC and TYR) in a tape water.

Conflicts of interest

There are no conflicts to declare.

Acknowledgements

Financial support from the Royal Society ACBI programme (Grant AQ150029) is gratefully acknowledged. HWL acknowledges the South African Research Chairs Initiative (SARChI) of the Department of Science and Innovation, and the National Research Foundation.

References

1 F. Carniato, G. Gatti and C. Bisio, *New J. Chem.*, 2020, **44**, 9969–9980.
2 C.-W. Chiu, T.-K. Huang, Y.-C. Wang, B. G. Alamani and J.-J. Lin, *Prog. Polym. Sci.*, 2014, **39**, 443–485.
3 M. K. Uddin, *Chem. Eng. J.*, 2017, **308**, 438–462.
4 A. Czımerová, J. Bujdák and A. Gáplovský, *Colloids Surf., A*, 2004, **243**, 89–96.
5 A. A. Adeyemo, I. O. Adeoye and O. S. Bello, *Appl. Water Sci.*, 2017, **7**, 543–568.
6 P. K. Ghosh and A. J. Bard, *J. Phys. Chem.*, 1984, **88**, 5519–5526.
7 R. Zhu, Q. Zhou, J. Zhu, Y. Xi and H. He, *Clays Clay Miner.*, 2015, **63**, 199–221.
8 M. Janek and G. Lagaly, *Colloid Polym. Sci.*, 2003, **281**, 293–301.
9 J. Kemmegne Mbouguen, E. Ngameni and A. Walcarius, *Anal. Chim. Acta*, 2006, **578**, 145–155.
10 J. K. Mbouguen, E. Ngameni and A. Walcarius, *Biosens. Bioelectron.*, 2007, **23**, 269–275.
11 M. C. N. Ngwem, J. C. Kemmegne-Mbouguen, H. W. Langmi, N. M. Musyoka and R. Mokaya, *ChemistrySelect*, 2022, **7**, e202202308.
12 J. C. K. Mbouguen, I. T. Kenfack, A. Walcarius and E. Ngameni, *Talanta*, 2011, **85**, 754–762.
13 J. C. Kemmegne-Mbouguen, L. Angnes, E. Mouafo-Tchinda and E. Ngameni, *Electroanalysis*, 2015, **27**, 2387–2398.
14 J. C. Kemmegne-Mbouguen and L. Angnes, *Sens. Actuators, B*, 2015, **212**, 464–471.
15 J. C. Kemmegne-Mbouguen, F. P. Tchoumi, E. Mouafo-Tchinda, H. W. Langmi, S. E. Bambalaza, N. M. Musyoka, C. Kowenje and R. Mokaya, *New J. Chem.*, 2020, **44**, 13108–13117.
16 A. D. Pournara, G. D. Tarlas, G. S. Papaefstathiou and M. J. Manos, *Inorg. Chem. Front.*, 2019, **6**, 3440–3455.
17 K. Kamal, M. A. Bustam, M. Ismail, D. Grekov, A. Mohd Shariff and P. Pré, *Materials*, 2020, **13**, 2741–2750.
18 Y.-R. Lee, J. Kim and W.-S. Ahn, *Korean J. Chem. Eng.*, 2013, **30**, 1667–1680.
19 A. Doménech, H. García, M. T. Doménech-Carbó and F. Llabrés-i-Xamena, *J. Phys. Chem. C*, 2007, **111**, 13701–13711.
20 J. Albo, D. Vallejo, G. Beobide, O. Castillo, P. Castaño and A. Irabien, *ChemSusChem*, 2017, **10**, 1100–1109.
21 J. M. Gonçalves, P. R. Martins, D. P. Rocha, T. A. Matias, M. S. S. Julião, R. A. A. Munoz and L. Angnes, *J. Mater. Chem. C*, 2021, **9**, 8718–8745.
22 T. Ma, H. Li, J.-G. Ma and P. Cheng, *Dalton Trans.*, 2020, **49**, 17121–17129.
23 W. Zhang, G. Jia, Z. Li, C. Yuan, Y. Bai and D. Fu, *Adv. Mater. Interfaces*, 2017, **4**, 1601241.
24 X. Wang, Q. Wang, Q. Wang, F. Gao, F. Gao, Y. Yang and H. Guo, *ACS Appl. Mater. Interfaces*, 2014, **6**, 11573–11580.
25 B. Peng, J. Cui, Y. Wang, J. Liu, H. Zheng, L. Jin, X. Zhang, Y. Zhang and Y. Wu, *Nanoscale*, 2018, **10**, 1939–1945.
26 D. M. Fernandes, A. D. S. Barbosa, J. Pires, S. S. Balula, L. Cunha-Silva and C. Freire, *ACS Appl. Mater. Interfaces*, 2013, **5**, 13382–13390.
27 M. Shabani-Nooshabadi, H. Karimi-Maleh and F. Tahernejad-Javazmi, *J. Electrochem. Soc.*, 2019, **166**, H218.

28 F. Boomsma, G. Alberts, F. A. J. van der Hoorn, A. J. Man in 't Veld and M. A. D. H. Schalekamp, *J. Chromatogr. B: Biomed. Sci. Appl.*, 1992, **574**, 109–117.
29 F. Patel, *Med., Sci. Law*, 1992, **32**, 303–310.
30 M. M. Rahman, N. S. Lopa, K. Kim and J.-J. Lee, *J. Electroanal. Chem.*, 2015, **754**, 87–93.
31 S. Wilson, D. Kamin and J. Feldman, *Clin. Chem.*, 1985, **31**, 1093–1094.
32 H. Y. Wang, Y. Sun and B. Tang, *Talanta*, 2002, **57**, 899–907.
33 W. Lohmann and U. Karst, *Anal. Bioanal. Chem.*, 2006, **386**, 1701–1708.
34 J. M. Wilson, J. T. Slattery, A. J. Forte and S. D. Nelson, *J. Chromatogr. B: Biomed. Sci. Appl.*, 1982, **227**, 453–462.
35 B. Habibi, M. Jahanbakhshi and M. H. Pournaghi-Azar, *Electrochim. Acta*, 2011, **56**, 2888–2894.
36 N. F. Atta and M. F. El-Kady, *Talanta*, 2009, **79**, 639–647.
37 J. Huang, Y. Liu, H. Hou and T. You, *Biosens. Bioelectron.*, 2008, **24**, 632–637.
38 J. C. Kemmegne-Mbouguen, I. T. Kenfack, A. Walcarius and E. Ngameni, *Talanta*, 2011, **85**, 754–762.
39 I. K. Tonle, E. Ngameni, D. Njopwouo, C. Carteret and A. Walcarius, *Phys. Chem. Chem. Phys.*, 2003, **5**, 4951–4961.
40 B. Narayana, M. Mathew, K. Vipin, N. V. Sreekumar and T. Cherian, *J. Anal. Chem.*, 2005, **60**, 706–709.
41 Y. Zhang, X. Bo, C. Luhana, H. Wang, M. Li and L. Guo, *Chem. Commun.*, 2013, **49**, 6885–6887.
42 J. Kim, S.-H. Kim, S.-T. Yang and W.-S. Ahn, *Microporous Mesoporous Mater.*, 2012, **161**, 48–55.
43 X. Mu, Y. Chen, E. Lester and T. Wu, *Microporous Mesoporous Mater.*, 2018, **270**, 249–257.
44 C.-M. Dai, J. Zhang, Y.-L. Zhang, X.-F. Zhou, Y.-P. Duan and S.-G. Liu, *Chem. Eng. J.*, 2012, **211–212**, 302–309.
45 V. E. Nicotra, M. F. Mora, R. A. Iglesias and A. M. Baruzzi, *Dyes Pigm.*, 2008, **76**, 315–318.
46 R. Senthil Kumar, S. Senthil Kumar and M. Anbu Kulandainathan, *Electrochem. Commun.*, 2012, **25**, 70–73.
47 M. Hartmann, S. Kunz, D. Himsl, O. Tangermann, S. Ernst and A. Wagener, *Langmuir*, 2008, **24**, 8634–8642.
48 L. D. O'Neill, H. Zhang and D. Bradshaw, *J. Mater. Chem.*, 2010, **20**, 5720–5726.
49 F. A. Sofi, M. A. Bhat and K. Majid, *New J. Chem.*, 2019, **43**, 3119–3127.
50 J. de Haro, A. Benítez, Á. Caballero and J. Morales, *Eur. J. Inorg. Chem.*, 2021, **2021**, 177–185.
51 M. Perfecto-Irigaray, J. Albo, G. Beobide, O. Castillo, A. Irabien and S. Pérez-Yáñez, *RSC Adv.*, 2018, **8**, 21092–21099.
52 M. Yadav, P. Singh, V. Ganesan, R. Gupta, P. K. Sonkar and D. K. Yadav, *Electroanalysis*, 2020, **32**, 248–257.
53 X. Kang, Y. Song, J. Zhao and Y. Li, *J. Electroanal. Chem.*, 2021, **895**, 115482.
54 A. R. Rajamani and S. C. Peter, *ACS Appl. Nano Mater.*, 2018, **1**, 5148–5157.
55 U. E. Majewska, K. Chmurski, K. Biesiada, A. R. Olszyna and R. Bilewicz, *Electroanalysis*, 2006, **18**, 1463–1470.
56 A. K. Vidyadharan, D. Jayan and T. Mary Nancy, *J. Solid State Electrochem.*, 2014, **18**, 2513–2519.
57 J. Chen, Y. Chen, S. Li, J. Yang, J. Dong and X. Lu, *Carbon*, 2022, **199**, 110–118.
58 M. Shabani-Nooshabadi, H. Karimi-Maleh and F. Tahernejad-Javazmi, *J. Electrochem. Soc.*, 2019, **166**, H218–H223.
59 H. Karimi-Maleh, M. Sheikhshoaie, I. Sheikhshoaie, M. Ranjbar, J. Alizadeh, N. W. Maxakato and A. Abbaspourrad, *New J. Chem.*, 2019, **43**, 2362–2367.
60 J. C. Kemmegne-Mbouguen and F. P. Tchoumi, *J. Solid State Electrochem.*, 2023, **27**, 939–953, DOI: **10.1007/s10008-022-05355-z**.
61 M. Taei and G. Ramazani, *Colloids Surf., B*, 2014, **123**, 23–32.
62 H. Karimi-Maleh, M. R. Ganjali, P. Norouzi and A. Bananezhad, *Mater. Sci. Eng. C*, 2017, **73**, 472–477.
63 J. C. Kemmegne-Mbouguen, H. E. Toma, K. Araki, V. R. L. Constantino, E. Ngameni and L. Angnes, *Microchim. Acta*, 2016, **183**, 3243–3253.
64 X. Chen, G. Zhang, Y. He, L. Shi, J. Zhang, G. Yang, H. Pan, W. Liu and S. Feng, *Int. J. Electrochem. Sci.*, 2020, **15**, 5927–5944.
65 Y. Luo, Y. Zhang, L. Lu and H. Luo, *J. Electroanal. Chem.*, 2020, **856**, 113737.
66 T. V. Gopal, T. M. Reddy, G. Venkataprasad, P. Shaikshavalli and P. Gopal, *Colloids Surf., A*, 2018, **545**, 117–126.
67 T. Madrakian, E. Haghshenas and A. Afkhami, *Sens. Actuators, B*, 2014, **193**, 451–460.
68 J. C. Kemmegne-Mbouguen and E. Ngameni, *Anal. Methods*, 2017, **9**, 4157–4166.
69 F. A. Sofi, M. A. Bhat and K. Majid, *New J. Chem.*, 2019, **43**, 3119–3127.
70 T. T. Minh, N. H. Phong, H. Van Duc and D. Q. Khieu, *J. Mater. Sci.*, 2018, **53**, 2453–2471.